Pushing the boundaries of chemistry? It takes #HumanChemistry

Make your curiosity and talent as a chemist matter to the world with a specialty chemicals leader. Together, we combine cutting-edge science with engineering expertise to create solutions that answer real-world problems. Find out how our approach to technology creates more opportunities for growth, and see what chemistry can do for you at:

evonik.com/career

EVONIK
Leading Beyond Chemistry

ADVANCED MATERIALS
www.advmat.de

Simultaneous Large Optical and Piezoelectric Effects Induced by Domain Reconfiguration Related to Ferroelectric Phase Transitions

Peter Finkel, Markys G. Cain, Thomas Mion, Margo Staruch, Jakub Kolacz, Sukriti Mantri, Chad Newkirk, Kyril Kavetsky, John Thornton, Junhai Xia, Marc Currie, Thomas Hase, Alex Moser, Paul Thompson, Christopher A. Lucas, Andy Fitch, Julie M. Cairney, Scott D. Moss, Alan Gareth Alexander Nisbet, John E. Daniels, and Samuel E. Lofland**

Electrical switching of ferroelectric domains and subsequent domain wall motion promotes strong piezoelectric activity, however, light scatters at refractive index discontinuities such as those found at domain wall boundaries. Thus, simultaneously achieving large piezoelectric effect and high optical transmissivity is generally deemed infeasible. Here, it is demonstrated that the ferroelectric domains in perovskite $Pb(In_{1/2}Nb_{1/2})O_3$–$Pb(Mg_{1/3}Nb_{2/3})O_3$–$PbTiO_3$ domain-engineered crystals can be manipulated by electrical field and mechanical stress to reversibly and repeatably, with small hysteresis, transform the opaque polydomain structure into a highly transparent monodomain state. This control of optical properties can be achieved at very low electric fields (less than 1.5 kV cm^{-1}) and is accompanied by a large (>10 000 pm V^{-1}) piezoelectric coefficient that is superior to linear state-of-the-art materials by a factor of three or more. The coexistence of tunable optical transmissivity and high piezoelectricity paves the way for a new class of photonic devices.

1. Introduction

Controlled switching of the optical properties of photonic materials has been utilized for numerous applications including optical filters, switches, and polarization control which has revolutionized telecommunications systems.[1] This has spurred the development of devices such as micrometer-sized piezoelectric optomechanical devices for quantum networks.[2] While exploitation of electromechanical resonances may enhance electro-optical performance,[3] sizable optical and piezoelectric responses in a single bulk material are highly unusual, even though there has been a continuing search for promising materials. One example is transparent ceramic

P. Finkel, T. Mion, M. Staruch, J. Kolacz, M. Currie, A. Moser
US Naval Research Laboratory
Washington, DC 02375, USA
E-mail: peter.finkel@nrl.navy.mil

M. G. Cain
Electrosciences Ltd.
Farnham GU9 9QT, UK

S. Mantri, J. E. Daniels
School of Materials Science and Engineering
University of New South Wales Sydney
Union Rd, Kensington, NSW 2052, Australia

C. Newkirk, K. Kavetsky, S. E. Lofland
Department of Physics
Rowan University
Glassboro, NJ 08028-1701, USA
E-mail: lofland@rowan.edu

The ORCID identification number(s) for the author(s) of this article can be found under https://doi.org/10.1002/adma.202106827.

DOI: 10.1002/adma.202106827

J. Thornton, S. D. Moss
Defence Science and Technology Group
Aerospace Division
Fishermans Bend, VIC 3207, Australia

J. Xia, J. M. Cairney
Department of Mechanical Engineering
University of Sydney
Sydney, NSW 2006, Australia

T. Hase
Department of Physics
University of Warwick
Conventry CV4 7AL, UK

P. Thompson, C. A. Lucas
Oliver Lodge Laboratory
Department of Physics
University of Liverpool
Liverpool L69 3BX, UK

P. Thompson, C. A. Lucas
XMaS Beamline
European Synchrotron Radiation Facility
Grenoble F-38043, France

A. Fitch
European Synchrotron Radiation Facility
71 Avenue des Martyrs, CS40220, Grenoble Cedex 9 38043, France

$Pb_{1-x}La_x(Zr_yTi_{1-y})O_3$ (PLZT)[4–7] which belongs to the family of piezoelectric phases based upon the prototypical relaxor $Pb(Zr_xTi_{1-x})O_3$ (PZT). However, Kumada et al.[8] showed that while the change in the light scattering by PLZT ceramics can be stimulated by antiferroelectric to ferroelectric phase transition,[9–11] it requires somewhat large electric fields of at least 5–10 kV cm^{-1} and has limited switching speed.[12,13] The lack of effective single-phase materials has led to recent efforts focused on piezoelectric–electrochromic composites to meet this design need for various sensors and devices.[14–16]

Recently, it became possible to grow large (centimeter size) single crystals[17] of the relaxor materials $Pb(Mg_{1/3}Nb_{2/3})O_3$–$PbTiO_3$ (PMN–PT) and $Pb(Zn_{1/3}Nb_{2/3})O_3$–$PbTiO_3$ which outperform conventional ceramic PZT-based materials due to extremely high piezoelectric ($d_{33} \approx 2000$ pm V^{-1}) and coupling ($k_3 \approx 0.9$) coefficients.[18–23] The success of these materials is due in part to domain engineering, a process used to modify the electric or mechanical response of a material through the manipulation of its domain configuration by cutting the crystals along certain crystallographic planes and then poling them with electric field along a particular crystallographic direction.

However, even after decades of development of lead-based relaxor ferroelectric crystals, there are still very few of them that produce simultaneous high piezoelectricity and optical transparency. While recent work on epitaxial piezoelectric thin films has demonstrated that they can be used as active optical devices[24] and that the ferroelectric domains give rise to nonlinear optical effects,[25] in bulk ferroelectric crystals, those domains cause light scattering due to discontinuities in the refractive index at the domain boundaries (domain walls).[26–28] The presence of many small domains (on the order of hundreds of nanometers) results in multiple scattering events which make the crystals opaque and have hindered the use of these materials in electro-optic applications. Eliminating domain walls leads to a mono-domain crystal with the maximum transparency, but this is generally at the expense of the piezoelectric efficiency.[29]

In one approach, Qiu et al.[30] reported a method of preparing a high-performance and nearly transparent relaxor piezoelectric using a special ac-poling process to create a favorable domain configuration that lacked 71° domain walls which scattered light in [001]-oriented rhombohedral PMN–PT. Though this process achieved good transparency and ultrahigh piezoelectricity, the optical properties of those crystals cannot be easily modulated. Only very recently, Deng et al.[31] demonstrated that domain-engineered rhombohedral crystals of PMN–PT can have large piezoelectric and electro-optic effects.

Here we show, for the first time, that domain-engineered crystals can provide broadly tunable optical properties while simultaneously realizing an extremely large piezoelectric response via a ferroelectric-to-ferroelectric phase transformation. The transition can be reversibly switched with an electric field of less than 1.5 kV cm^{-1} and is accompanied by a large strain of up to 0.25%, yielding an effective giant piezoelectric coefficient >10 000 pm V^{-1}. The transmissivity of light through the crystal can be varied from <~1% to ~70%, and the rise time can be as small as a few tens of microseconds. By using various in situ X-ray techniques, combined with spectral analysis and high-speed videography, we establish the mechanism for this effect as light scattering due to the polydomain state formed during the initial poling. This discovery opens possibilities to incorporate the giant control of transmissivity due to optical scattering by ferroelectric domains and concomitant piezoelectric effects into novel advanced electro-optical devices and applications.

A. G. A. Nisbet
I16 Beamline
Diamond Light Source
Oxfordshire OX11 0DE, UK

2. Results and Discussion

We selected xPb$(In_{1/2}Nb_{1/2})O_3$–$(1-x-y)$Pb$(Mg_{1/3}Nb_{2/3})O_3$–yPbTiO$_3$ (PIN–PMN–PT) with $x \approx 0.24$ and $y \approx 0.30$. At this composition, the rhombohedral R phase is stabilized at zero field and stress at room temperature close to the morphotropic phase boundary,[32–34] and the transition to the orthorhombic O phase can take place with relatively small mechanical and/or electrical excitation along the appropriate directions.[35–37] The as-grown pseudocubic ferroelectric crystals with rhombohedral symmetry have 8 equivalent polarization directions, each along the <111> type axes. To implement domain engineering, the crystal was first cut along orthogonal (011), (01$\bar{1}$), and (100) faces with final dimensions $4 \times 4 \times 12$ mm^3, respectively, and then it was poled along [011]. After poling, only two variants of the rhombohedral (R) phase remain with the polarization along either [111] or [$\bar{1}$11]. Mechanical compatibility should then require that the domains be separated by 71° or 109° domain walls[38] oriented parallel to (100) or (011), respectively. As expected, the resulting as-poled crystals exhibited twinning, which can lead to ambiguity in the interpretation of X-ray diffraction results. However, we confirmed that the crystals possessed R symmetry with space group $R3m$ at zero field and zero stress (Figure S1, Supporting Information).

All measurements were performed with uniaxial compressive stress applied along the [100] long axis and the electric field $E \parallel$ [011], while optical experiments were conducted with light propagating along [01$\bar{1}$] (**Figure 1**a, inset). Optical transmission measurements with a sinusoidal electric field of frequency 1 Hz and amplitude 1.25 kV cm^{-1} and increasing stress are shown in Figure 1a with the gray and black markers corresponding to the maximua and minima in the electric field, respectively. The light transmission increased with compressive stress, especially when it exceeded −20 MPa, corresponding with an anomaly in the stress–strain curve (Figure 1a). In this region, the effective piezoelectric coefficient $d_{32}^* = \Delta\varepsilon/\Delta E >$ 10 000 pm V^{-1} (Figure S2 and Table S1, Supporting Information), almost an order of magnitude higher than the sizable value of the crystal in the as-poled R state (≈1500–2000 pm V^{-1}). The striking change in the appearance of the crystal can be seen from photographs taken at high and low stresses (Figure 1b,c), and repeatable electrical switching is shown in Figure 1d.

Pursuant to investigating the underlying structural properties responsible for the observed optical effects reported above, in situ X-ray diffraction and synchrotron-based diffuse multiple scattering (DMS) were performed (see the Experimental Section). These two techniques provide unique, complementary insight into the crystal structure even for polydomain

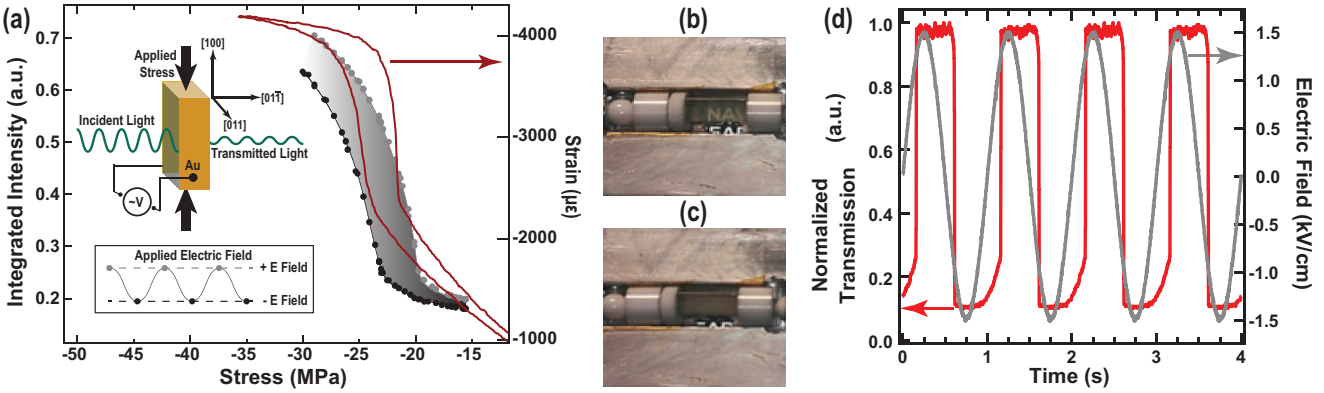

Figure 1. a) Stress dependence of the integrated transmitted light intensity and strain. The measurements were done with a high-speed video camera with the sample illuminated with a wide spectrum white LED source while an ac electric field was applied, and the gray and black dots correspond to the maximum and minimum electric fields, respectively. The inset shows a schematic of the setup for the transmittance measurements. b,c) Photographs of the crystal at high stress (b) and low stress (c), showing the marked difference in transmission. d) Time-dependent optical relative normalized transmission of 730 nm radiation through the sample along the [01 $\bar{1}$] direction measured by a high-speed photodetector, showing the repeatable and reversible nature of the effect for a crystal under ≈22 MPa compressive stress.

states. Stress-dependent X-ray diffraction data are displayed in **Figure 2**a,b for the (022) and (111) diffraction peaks, respectively. The polarization was monitored with a high-impedance electrometer during the measurement, yielding so-called "open-circuit" electrical boundary conditions which caused the transition to shift to larger compressive stress (Figure 2b, inset) as compared to that of the short-circuit data shown in Figure 1a. The position of the (022) diffraction peak center displayed clear hysteresis with application and removal of stress and correlated directly with the measured strain. On loading, the response deviated from linear behavior near a compressive stress of 30 MPa, at which point the crystal transformed to a monoclinic phase, presumably M_B based on symmetry arguments, and the two peaks coalesced into one when the compressive stress exceeded ≈35 MPa, as clearly seen in the reciprocal space maps of the (111) reflection at low and high stresses (Figure 2b insets and Figure S3 (Supporting Information)).

DMS is a divergent beam diffraction technique that produces diffraction cones which have a solid angle determined by the lattice *d*-spacing and impinge upon the detector plane in the form of lines. When three cones from coplanar reflections intersect at a common point, this is referred to as a triple intersection (TI) and has the property that it can only be split if at least one angle in the Bravais lattice deviates from 90°. By calculating the splitting for the Bravais systems over multiple TIs, a splitting fingerprint can be generated and used for phase identification. The DMS analysis here involved three sets of TIs from coplanar reflections (Figure S4, Supporting Information). The presence of parallel lines at low stress indicates two phases. The splitting of the TIs precludes cubic, tetragonal, and orthorhombic structures. Comparing the splitting fingerprints (green and orange, Figure S4a, Supporting Information) for the low-stress data (Figure 2c) revealed two rhombohedral phases rotated from one other by 90°, indicating a rotation of the polarization of about 70.5° between neighboring domains. With increased compressive stress, the two rhombohedral twins changed to a twinned monoclinic structure. At even higher stress, the twins collapsed to a single phase (Figure 2d and Figure S4a, Supporting Information, yellow fingerprint), which we have designated as M* as it could only be described by monoclinic or lower symmetry.

Both the X-ray diffraction and DMS results suggest a transition from a poly- to a monodomain state. For confirmation, we performed high-energy (80 kV) X-ray diffuse scattering to characterize the local disorder throughout the bulk of the crystals since the method is especially sensitive to discontinuities in the long-range atomic periodicity.[39] Diffuse scattering measurements were done at zero stress with varying electric fields, where **Figure 3**a shows the diffuse scattering structure around a (002) diffraction spot measured at zero and high fields. There was streaking of the reciprocal lattice point observed along the <551> directions at zero field that results from planar interfaces within the crystal perpendicular to these directions. For lead-based relaxor ferroelectrics, such diffuse scattering streaks have been regularly observed and have been modeled as polar nanoregions[40–42] or planar structures akin to conventional domains but nanoscale in size,[43] though other models have also been proposed,[44] but the present streaking at zero field is consistent with conventional planar domain walls. On the other hand, at high field (Figure 3a), the streaks were removed, i.e., the diffuse scattering was nearly symmetrical around the reciprocal lattice point as the domain walls had been removed (Figure S5, Supporting Information), as required for a monodomain crystal.[45,46]

For further study of the domain structure, transmission electron microscopy (TEM) with in situ compression (Figure S6, Supporting Information) was completed on a lamella cut from one of the crystals.[47] Figure 3b shows <111> nanodomains within the polydomain rhombohedral structure of the lamella prior to loading. Under sufficient compression (Figure 3c), the nanodomains disappeared during the transition to form a monodomain state. While finite size effects play a role in the domain microstructure such that the present TEM results are expected to differ from those of the bulk crystal, the behavior should be qualitatively similar.

An image of the light transmitted through the crystal during decreasing compressive stress is shown in Figure 3d. The black lines show the time evolution of the boundary of the region of light transmission. The direction of motion of the edges of the region (shown by the light blue arrows) coincided with the direction of the streaking in the diffuse scattering by the domain walls (Figure 3a), directly linking the ferroelectric domain structure in the R phase to the reduced optical transmission.

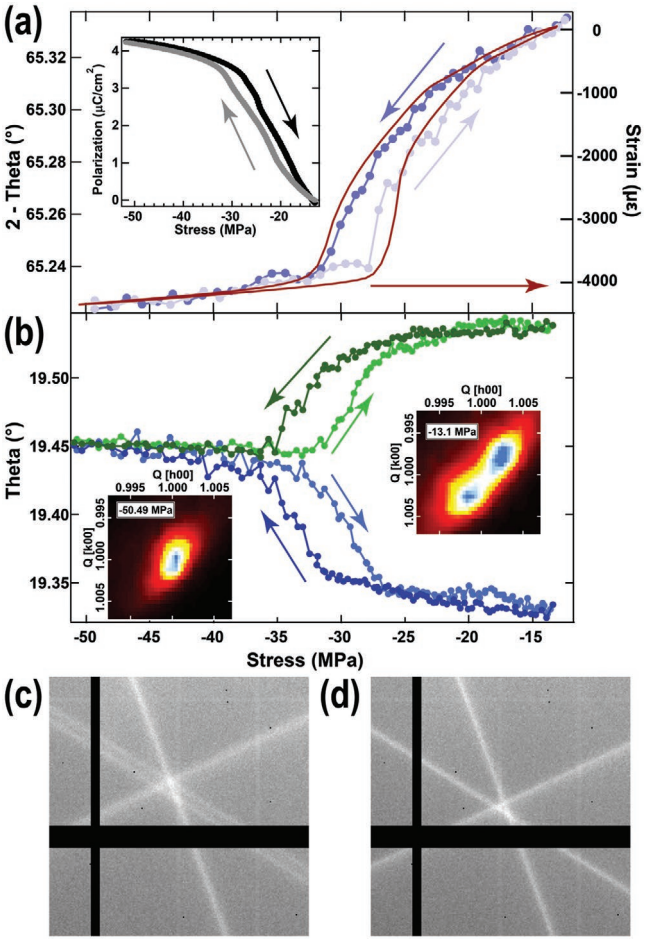

Figure 2. a,b) Evolution of the (220) (a) and (111) (b) peaks during loading and unloading cycles. Also included in (a) is the stress–strain curve and the polarization (inset). Reciprocal space map image plots for the (111) peak at low and high stress are shown as insets in (b). Note, we adopt the traditional engineering convention of compressive stress to be negative. c,d) DMS results at low stress, zero-field (–7 MPa) (c) and high stress, high field (–24 MPa, 2.5 kV cm^{-1}) (d) states. At low stress, there are two rhombohedral phases that become monoclinic with increasing stress and eventually merge into a single phase at high stress.

The spectral transmittance was measured across the region spanning the ultraviolet to the near-infrared with and without a compressive load (**Figure 4**a). When placing the sample 0.6 m away from the detector, the transmitted light through the unloaded sample diminished substantially in the visible region as compared to when the detector abutted the sample. Under a compressive stress of 40 MPa, the signal was independent of detector placement, and the transmittance was effectively constant for wavelength $\lambda > 800$ nm. While the unloaded sample tended to show decreased transmittance compared to the loaded sample, near the mid-infrared region, the transmissivity was nearly independent of the measurement conditions. Additional studies with incident polarized light showed similar spectral characteristics which were independent of the polarization direction.

The transmittance T of light through a medium is generally described by Beer's law

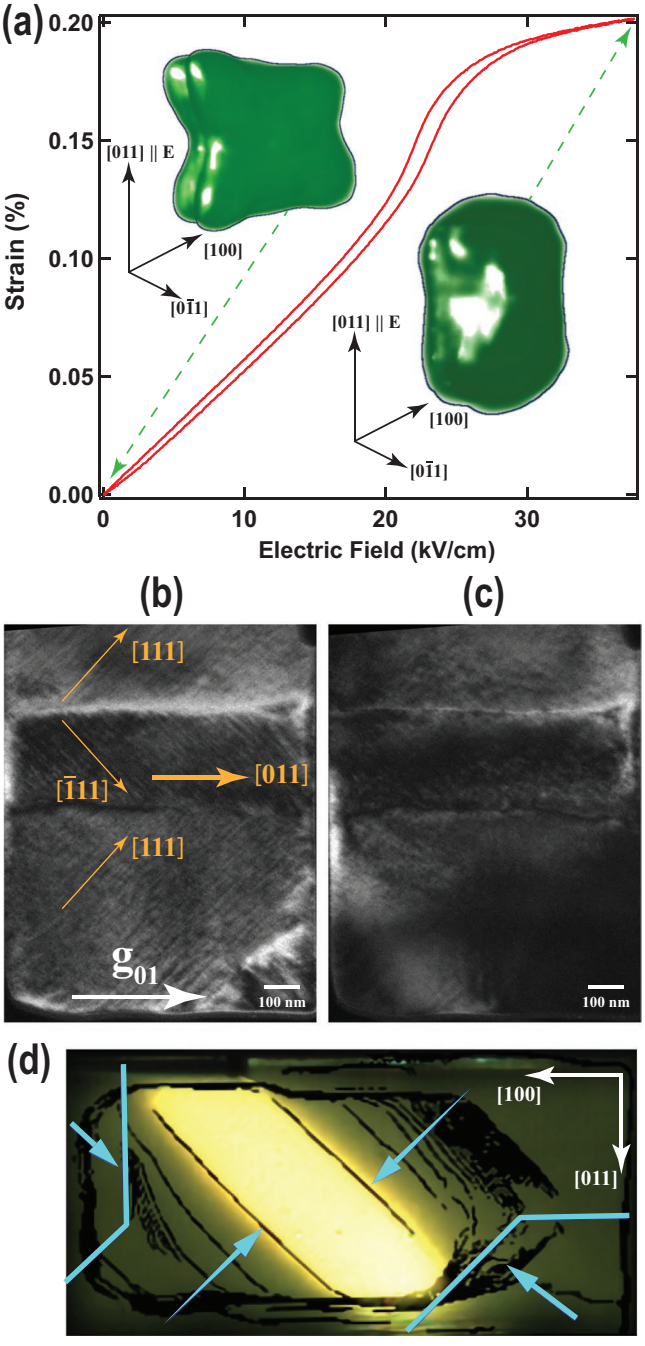

Figure 3. a) Electric field dependence of the strain, indicating the phase transition at ≈23 kV cm^{-1} with zero applied stress. The insets display the diffuse scattering structure around the (002) reflection in the zero-field state and the high-field state (≈38 kV cm^{-1}). Eight streaks emanating from the reciprocal lattice spot (see Figure S5 in the Supporting Information) disappeared when the crystal transitioned to the high-field symmetry. b,c) TEM images of a lamella cut from single crystal under zero (b) and high (c) compressive stresses. Large stress promoted the disappearance of twinned nanodomains along the [111] and [$\bar{1}$11] directions observed in the unloaded lamella. The contrast observed at high stress is attributed to the nonuniform stress from the nanoindenter. d) Time evolution of the white-light transmission through a crystal during unloading measured by high-speed video (see the Supporting Information). The black lines indicate the boundaries of the bright regions at various times, and the light blue arrows indicate the motion of those boundaries.

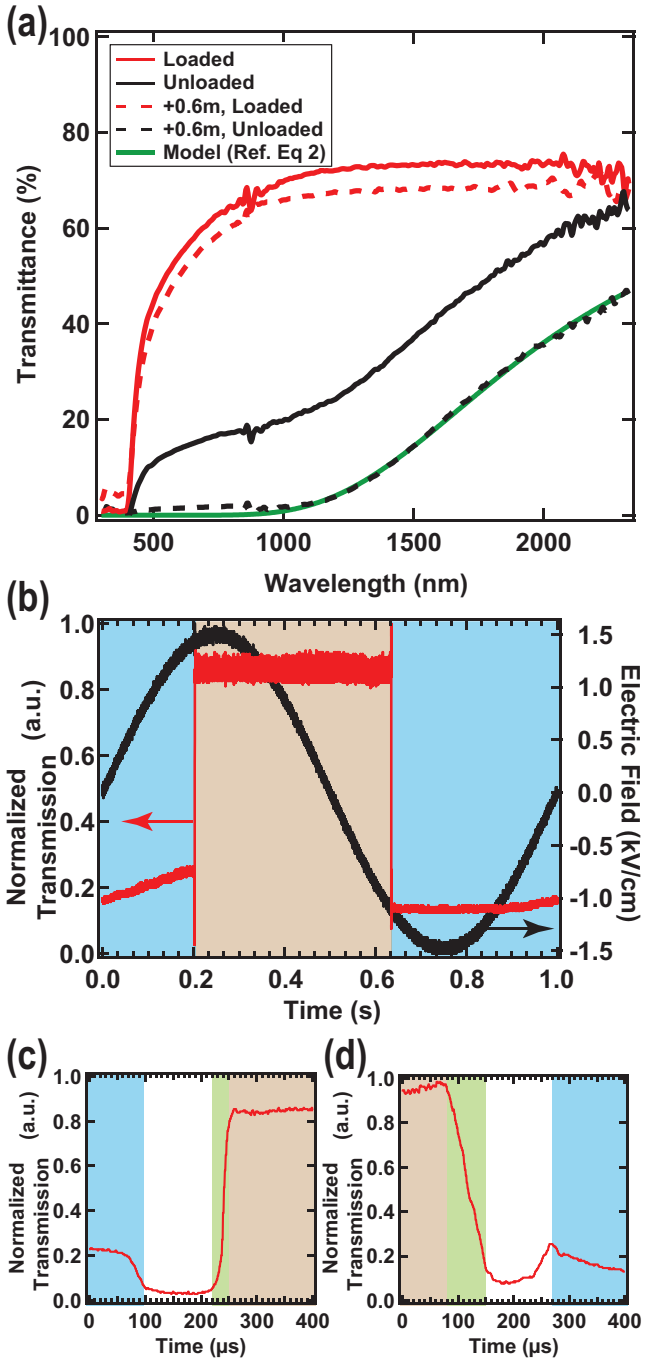

Figure 4. Optical transmittance of a relaxor ferroelectric PIN–PMN–PT single crystal. a) Light transmittance for a crystal under zero (black) and –40 MPa (red) stresses measured at the sample and 0.6 m away. The green line represents a fit to Equation (2). b) Time dependence of the normalized transmission (red) at 730 nm with a 1 Hz ac electric field of amplitude 1.5 kV cm^{-1} (black) at a compressive stress of 20 MPa. c,d) Detailed views of the regions of discontinuity in the optical transmission in (b), i.e., during increasing and decreasing electric fields, respectively. There are 3 distinct regions (blue, red, and white), each related to a different crystal structure. The transitions between opaque and transparent states are shaded green.

$$T = T_0 e^{-\alpha l} \tag{1}$$

where T_0 is the transmittance into the medium, α is the attenuation coefficient, and l is its thickness. While single crystals of sapphire and titania are transparent, their fully dense ceramics are opaque or translucent. This has been attributed to scattering due to the differences in the extraordinary and ordinary indices of refraction, n_e and n_o, respectively, in birefringent media and has been successfully modeled by Pecharromán et al.[48] by modifying Rayleigh–Gantz–Debye (RGD) theory to account for crystal orientation

$$\alpha = \frac{3}{2d} g(\psi)(m-1)^2 \left\{\frac{5}{2} + 2x^2 - sinc\,4x - \frac{7}{16x^2(1-\cos 4x)} - \left(2 - \frac{1}{2x^2}\right)[\gamma + \ln 4x - Ci(4x)]\right\} \tag{2}$$

where d is the grain size, ψ is the angle between the direction of light propagation and the optical axis, $g(\psi)$ is a function to account for scattering due to orientation of the optical axis, $m = n_e/n_o$, $x = \pi \langle n \rangle d/\lambda$ with $\langle n \rangle$ being the average index of refraction, $\gamma = 0.577...$ (the Euler–Mascheroni number), and Ci(x) the cosine integral function. For the present case, $g(35°) = 0.1389$. While $\langle n \rangle$ must show dispersion, the transmittance of the loaded sample remains constant at ≈70% from 1000 to 2500 nm. The Fresnel equations indicate that $\langle n \rangle \approx 2.5$ in that region, consistent with measurements on similar crystals.[49–51] The resulting fit to Equation (2) is quite satisfactory (green line, Figure 4a), yielding values of $d = 240 \pm 20$ nm and $m = 1.016 \pm 0.002$. The measured refractive indices of rhombohedral single crystals of PIN–PMN–PT with similar composition gave $m \approx 1.016$ at $\lambda = 475$ nm in one study[31] and $m \approx 1.026$ at $\lambda = 633$ nm in another.[51] One should expect that the fit values for domain size d should differ somewhat from the actual values as RGD theory was strictly derived for spherical particles,[52] but they are in good agreement with previous studies by us[47] and others[53,54] which indicate domain sizes in the range of a couple of hundred nanometers up to 1 μm in these and similar crystals.

Time-resolved optical transmission measurements (Figure 4b–d) of 730 nm radiation through the sample preloaded close to the phase transition (≈–20 MPa) highlight three distinct states with different degrees of opacity. Starting from the initial as-poled state (Figure 4c) in stage 1 (blue shaded region), the transmittance showed a weak dependence on electric field. With increasing electric field, there was a marked reduction in the transmittance at 1.4 kV cm^{-1} during the transient state 2 (Figure 4c, unshaded region), which was immediately followed by a rapid 30 μs change (green shaded region) to transparency in state 3 (red shaded region). The crystal remained in state 3 until the switching was reversed with decreasing field at about –1.1 kV cm^{-1} with slight differences in the field dependence of the transmittance. These three optical states correspond to the three structural phases we have identified. The polydomain R phase (state 1) scatters light due to the birefringence responsible for the refractive index mismatch at the twin boundaries, but each domain produces only one extraordinary ray due to the uniaxial crystal symmetry. However, the twinned, lower symmetry monoclinic M_B phase in state 2 has two extraordinary

rays, thereby enhancing the scattering and reducing the transmission. When the domain walls collapse to form a monodomain crystal in the M* phase (state 3), light at normal incidence propagates along an optical axis so that even though the phase remains birefringent, there are no extraordinary rays. The dip in transmittance due to the M_B phase was not observed in the high-speed video (Figure 1a) because the effect is strongly wavelength-dependent and was washed out with a broadband white light source.

In previous research, it was shown that there was no visible degradation of the piezoelectric performance over tens of million cycles[55] which was attributed to a flat energy landscape that facilitates switching.[56,57] Even so, this durability is counter to the fact that insulating crystals such as these are naturally susceptible to brittle failure and cracking, especially since Landau theory[58] dictates that the transition from $R3m$ to M_B cannot be continuous. The present twinning/detwinning process closely resembles displacive martensitic transformations that lead to stress accommodation and adaptive compatibility of multiple phases,[59–61] and the M_B phase may serve to span the differences between the structures of R and M* phases. This adaptive behavior is likely also linked to another important aspect of these crystals, their minimal electromechanical hysteresis. The domain walls found in the as-poled crystal are identified by diffuse scattering analysis as existing on {551}-type planes. In pure R-type materials, these wall orientations would be charged and strained, leading to increased electrostatic and mechanical mismatch energy.[62,63] For monoclinic phases, such planes can represent the lowest strain energy state,[63] even when electrical poling creates charged walls.

3. Conclusion

We have demonstrated high optical modulation with simultaneous giant piezoelectricity by engineering and controlling the domain configuration and phase by stress or electric field in a ferroelectric crystal. The optical transmission through the crystal is determined by light scattering from the ferroelectric domains, correlated to the inter-ferroelectric phase transitions, which are responsible for the large strain and can achieve relatively fast switching (<30 µs). An intermediate monoclinic structure and an adaptive phase transition combined with metastable charged domain walls contribute to small hysteresis as well as resistance to fatigue. This hysteretic behavior with applied electric field or stress also suggests the possibility of controlling the remanent state of the crystal to either be opaque or transparent, opening new venues for novel functionalities and applications. While hysteretic effects may limit applications due to potential self-heating, previous investigation[64] suggests that the hysteresis is sufficiently narrow as to alleviate that concern even for high power. These results have the potential to impact multiple disciplines including photovoltaics, optoelectronics, and ferroelectric memories.

4. Experimental Section

In Situ High-Speed Video: High-speed video acquisition was made with a high-resolution Phantom v711 camera with exposure times ranging from 10 µs to 1 ms at rates of up to 50 000 frames s^{-1}. The crystal was placed in custom-built fixture in an Instron testing unit, and the electric potential was applied with a Trek 10/10B amplifier. A broadband light-emitting diode (LED) array illuminated the crystal with light propagating along $[01\bar{1}]$ direction, as diagramed in Figure 1a inset, and the strain was measured with a strain gauge attached to the (011) surface in the [100] direction.

Optical Modulation: The sample was mounted in a custom-built 1000 N compression holder, which used a micrometer screw to manually apply force which was measured with a load cell. The holder was positioned to center the sample between a 30-mW 730-nm laser and a 2-GHz Si free-space high-speed photodetector, with light transmission along the $[01\bar{1}]$ axis of the crystal. To reduce the influence of scattered light, the detector was positioned 0.5 m from the detector head. The electric potential was applied by a Trek 609E-6 high-voltage amplifier, which was driven by a Wavetek 395 waveform generator. The photodetector output, with a 50-Ω feed-through termination, and the voltage monitor from the high-voltage amplifier were connected to a Teledyne Lecroy oscilloscope.

In Situ X-ray Diffraction: Synchrotron X-ray diffraction measurements were performed at European Synchrotron Radiation Facility (ESRF). Reciprocal space maps and line scans were collected with an offline lab-based setup at ESRF beamline BM28 with Cu K_α ($\lambda = 1.5406$ Å) radiation and a custom fixture designed to apply stress as well as electrical field. Strain was monitored during diffraction measurements by a strain gauge affixed to the $(0\bar{1}1)$ crystal face and aligned along the [100] direction. Other details were described elsewhere.[65,66] A Maxipix 2D camera was used to align and orient the crystal, and subsequently it was used to obtain reciprocal space maps, allowing full 3D reconstruction of the reciprocal space.

Synchrotron X-ray diffraction measurements used for Rietveld refinement were performed at ESRF beamline ID22 with 35 keV ($\lambda = 0.35424$ Å) radiation with a specially designed rotational apparatus. The apparatus allowed rotation of the crystal along two axes during acquisition of the 2θ diffraction intensity at room temperature whereby all diffraction peaks were measured in transmission geometry. A multianalyzer stage consisting of 9 analyzers was mounted with individually corresponding Si (111) crystals used to reduce aberrations compared to a Soller slit. Rietveld refinement was performed with GSAS II software.

Diffuse Multiple Scattering: The sample was mounted on a Newport kappa geometry diffractometer on the I16 beamline at Diamond Light Source synchrotron. The sample was connected to a Trek high-voltage power supply. The sample was oriented with two Bragg reflections to build a *UB* orientation matrix where the *B* matrix transformed a given (*hkl*) to an orthonormal coordinate system fixed in the crystal and the *U* matrix was a rotation matrix that rotated the crystal's reference frame to that of the diffractometer. The sample was then orientated to a noninteger (*hkl*) to project a precalculated set of DMS lines forming triple intersections in the cubic setting, onto the detector. An electric field was cycled at various compressive stress loads. More details can be found in the Supporting Information and ref. [67].

Diffuse X-ray Scattering: Diffuse X-ray scattering data were collected at the Imaging and Medical Beamline (IMBL) of the Australian Synchrotron. A beam energy of 79.7 keV was used with a sample to detector distance of 633 mm. Scattered intensities were recorded with a Hamamatsu flat panel detector to a maximum q-range of 5 $Å^{-1}$. The crystal was mounted in a Critus in situ electrical loading cell,[46] allowing the macroscopic strain to be recorded simultaneously with the collection of diffuse X-ray scattering data. Data were collected during a crystal rotation from –40° to 55°. The detector intensities were then resampled into reciprocal space coordinates with isosurface renderings being produced by the software package Dragonfly.[68]

Optical Transmittance under Stress: Optical transmittance measurements were performed with a Perkin Elmer 1080 spectrophotometer with a 150 mm integrating sphere and UV–vis–IR detector. The transmittance data were collected with the sample in two positions: 1) the sample placed at the input port of the integrating sphere and 2) the sample placed in the

beam path but 0.6 m in front of the integrating sphere. A custom mount allowed application of a uniaxial mechanical load to the sample without interfering with the optical beam path.

Transmission Electron Microscopy: A crystal was cut to create a 0.5 mm plate that was thinned into a wedge shape with a tripod polisher. After fixing to a copper mount, the wedge was milled with a Zeiss Auriga focused ion beam fabrication into an $\approx 200 \times 900 \times 1200$ nm^3 section. Microscopy was done with JEOL 2100 TEM operating at 200 kV, and in situ uniaxial compression was performed with a Hysitron PI 95 diamond nanoindentor.

Supporting Information

Supporting Information is available from the Wiley Online Library or from the author.

Acknowledgements

Funding for this work was provided by the Office of Naval Research (ONR) under Contract No. N001421WX01058. This work was supported in part by the American Society for Engineering Education Fellowship. M.C. acknowledges support by core programs at the U.S. Naval Research Laboratory funded by ONRG. Funding for this work (J.E.D.) was provided by the Office of Naval Research (ONR) under Award Number N62909-19-1-2090. This was also supported by the Australian Federal Government through the Next Generation Technologies Fund, and the Strategic Research Initiative in Advanced Materials and Sensors. The authors are grateful for the scientific and technical support from the Australian Centre for Microscopy and Microanalysis, the Microscopy Australia (MA) node at the University of Sydney. Parts of this research work was carried out in the framework of the ADVENT project (Grant Number: 16ENG06 ADVENT) which is supported by the European Metrology Programme for Innovation and Research (EMPIR). The EMPIR initiative is cofunded by the European's Horizon 2020 research and innovation programme and the EMPIR Participating States. XMaS, BM28, is a UK National Research Facility funded by EPSRC. The authors acknowledge the European Synchrotron Radiation Facility for X-ray diffraction experiments performed on beamline ID-22, Diamond Light Source for time on beamline I16 under proposal MM18924-1 to perform DMS experiments, and the IMBL beamline at the Australian Synchrotron, part of ANSTO, for the diffuse scattering studies. This article has been contributed to by US Government employees and their work is in the public domain in the USA.

Conflict of Interest

The authors declare no conflict of interest.

Data Availability Statement

The data that support the findings of this study are available from the corresponding author upon reasonable request.

Keywords

electrochromic composites, piezoelectric activity, single crystals, X-ray diffraction

Received: August 29, 2021
Revised: October 31, 2021
Published online:

[1] D. A. B. Miller, *J. Lightwave Technol.* **2017**, *35*, 346.
[2] W. Jiang, C. J. Sarabalis, Y. D. Dahmani, R. N. Patel, F. M. Mayor, T. P. McKenna, R. van Laer, A. H. Safavi-Naeini, *Nat. Commun.* **2020**, *11*, 1166.
[3] J. Li, Y. Li, Q. Meng, Z. Zhou, D. Jia, R. McIntosh, A. S. Bhalla, R. Guo, *Mater. Res. Bull.* **2018**, *97*, 523.
[4] G. H. Haertling, *J. Am. Ceram. Soc.* **1999**, *82*, 797.
[5] G. H. Haertling, C. E. Land, *J. Am. Ceram. Soc.* **1971**, *54*, 1.
[6] K. Nashimoto, S. Nakamura, T. Morikawa, H. Moriyama, M. Watanabe, E. Osakabe, *Jpn. J. Appl. Phys.* **1999**, *38*, 5641.
[7] C. E. Land, P. D. Teacher, G. H. Haertling, in *Applied Solid State Science* (Ed: W. Raymond), Elsevier, Amsterdam, The Netherlands **1974**, pp. 137–233.
[8] A. Kumada, K. Suzuki, G. Toda, *Ferroelectrics* **1976**, *10*, 25.
[9] C. Kittel, *Phys. Rev.* **1951**, *82*, 729.
[10] S.-E. Park, M.-J. Pan, K. Markowski, S. Yoshikawa, L. E. Cross, *J. Appl. Phys.* **1998**, *82*, 1798.
[11] I. V. Ciuchi, L. Mitoseriu, C. Galassi, *J. Am. Ceram. Soc.* **2016**, *99*, 2382.
[12] A. Kumada, G. Toda, Y. Otomo, *Ferroelectrics* **2011**, *7*, 367.
[13] W. Ruan, G. Li, J. Zeng, J. Bian, L. S. Kamzina, H. Zeng, L. Zheng, A. Ding, *J. Am. Ceram. Soc.* **2010**, *93*, 2128.
[14] Z. He, B. Gao, T. Li, J Liao, B. Liu, X. Liu, C. Wang, Z. Feng, Z. Gu, *ACS Sustainable Chem. Eng.* **2019**, *7*, 1745.
[15] X. Chen, L. Luo, Z. Zeng, J. Jiao, M. Shehzad, G. Yuan, H. Luo, Y. Wang, *J. Materiomics* **2020**, *6*, 643.
[16] S. Qin, Q. Zhang, X. Yang, M. Liu, Q. Sun, Z. L. Wang, *Adv. Energy Mater.* **2018**, *8*, 1800069.
[17] S. E. E. Park, W. Hackenberger, *Curr. Opin. Solid State Mater. Sci.* **2002**, *6*, 11.
[18] S. Zhang, T. R. Shrout, *IEEE Trans. Ultrason., Ferroelectr., Freq. Control* **2010**, *57*, 2138.
[19] H. Fu, R. E. Cohen, *Nature* **2000**, *403*, 281.
[20] S.-E. Park, T. R. Shrout, *J. Appl. Phys.* **1998**, *82*, 1804.
[21] E. Sun, W. Cao, *Prog. Mater. Sci.* **2014**, *65*, 124.
[22] F. Li, S. Zhang, J. Luo, X. Geng, Z. Xu, T. R. Shrout, *J. Appl. Phys.* **2016**, *120*, 074105.
[23] H. Qiao, C. He, Z. Wang, X. Li, Y. Liu, H. Tailor, X. Long, *J. Am. Ceram. Soc.* **2019**, *102*, 79.
[24] S. Abel, T. Stöferle, C. Marchiori, C. Rossel, M. D. Rossell, R. Erni, D. Caimi, M. Sousa, A. Chelnokov, B. J. Offrein, J. Fompeyrine, *Nat. Commun.* **2013**, *4*, 1671.
[25] M. F. Sarott, M. Fiebig, M. Trassin, *Appl. Phys. Lett.* **2020**, *117*, 132901.
[26] G. F. Nataf, M. Guennou, *J. Phys.: Condens. Matter* **2020**, *32*, 183001.
[27] L. W. Martin, A. M. Rappe, *Nat. Rev. Mater.* **2016**, *2*, 1671.
[28] Y. Zhang, W. Jie, P. Chen, W. Liu, J. Hao, *Adv. Mater.* **2018**, *30*, 1707007.
[29] D. Damjanovic, *J. Am. Ceram. Soc.* **2005**, *88*, 2663.
[30] C. Qiu, B. Wang, N. Zhang, S. Zhang, J. Liu, D. Walker, Y. Wang, H. Tian, T. R. Shrout, Z. Xu, L.-Q. Chen, F. Li, *Nature* **2020**, *577*, 350.
[31] C. Deng, L. Ye, C. He, G. Xu, Q. Zhai, H. Luo, Y. Liu, A. J. Bell, *Adv. Mater.* **2021**, *33*, 2663.
[32] A. Amin, M. J. Haun, B. Badger, H. McKinstry, L. E. Cross, *Ferroelectrics* **2011**, *65*, 107.
[33] A. Amin, L. E. Cross, *Br. Ceram. Trans.* **2013**, *103*, 89.
[34] D. Damjanovic, *Appl. Phys. Lett.* **2010**, *97*, 062906.
[35] D. Viehland, J. F. Li, *J. Appl. Phys.* **2002**, *92*, 7690.
[36] P. Finkel, M. Staruch, A. Amin, M. Ahart, S. E. Lofland, *Sci. Rep.* **2015**, *5*, 13770.
[37] Y. Wang, D. Wang, G. Yuan, H. Ma, F. Xu, J. Li, D. Viehland, P. M. Gehring, *Phys. Rev. B* **2016**, *94*, 174103.
[38] J. Fousek, V. Janovec, *J. Appl. Phys.* **1969**, *40*, 135.
[39] T. R. Welberry, *Diffuse X-Ray Scattering and Models of Disorder*, Oxford University Press, New York **2004**.

[40] G. Xu, Z. Zhong, H. Hiraka, G. Shirane, *Phys. Rev. B* **2004**, *70*, 174109.
[41] T. R. Welberry, M. J. Gutmann, H. Woo, D. J. Goossens, G. Xu, C. Stock, W. Chen, Z.-G. Ye, *J. Appl. Crystallogr.* **2005**, *38*, 639.
[42] I.-K. Jeong, T. W. Darling, J. K. Lee, T. Proffen, R. H. Heffner, J. S. Park, K. S. Hong, W. Dmowski, T. Egami, *Phys. Rev. Lett.* **2005**, *94*, 147602.
[43] M. Eremenko, V. Krayzman, A. Bosak, H. Y. Playford, K. W. Chapman, J. C. Woicik, B. Ravel, I. Levin, *Nat. Commun.* **2019**, *10*, 2728.
[44] M. J. Krogstad, P. M. Gehring, S. Rosenkranz, R. Osborn, F. Ye, Y. Liu, J. P. C. Ruff, W. Chen, J. M. Wozniak, H. Luo, O. Chmaissem, Z.-G. Ye, D. Phelan, *Nat. Mater.* **2018**, *17*, 718.
[45] G. Xu, Z. Zhong, Y. Bing, Z.-G. Ye, G. Shirane, *Nat. Mater.* **2006**, *5*, 134.
[46] J. Daniels, "Critus XRD | Diffraction with Electric Field," https://www.critus.com.au/ (accessed: October 2021).
[47] Y. Liu, J. Xia, P. Finkel, S. D. Moss, X. Liao, J. M. Cairney, *Acta Mater.* **2019**, *175*, 436.
[48] C. Pecharromán, G. Mata-Osoro, J. S. Moya, L. A. Díaz, R. Torrecillas, *Opt. Express* **2009**, *17*, 6899.
[49] F. Wu, B. Yang, E. Sun, W. Yang, W. Cao, *Opt. Mater.* **2013**, *36*, 342.
[50] X. Wan, H. L. W. Chan, C. L. Choy, X. Zhao, H. Luo, *J. Appl. Phys.* **2004**, *96*, 1387.
[51] F. Wu, B. Yang, E. Sun, G. Liu, H. Tian, W. Cao, *J. Appl. Phys.* **2013**, *114*, 027021.
[52] D.-S. Wang, P. W. Barber, *Appl. Opt.* **1978**, *17*, 797.
[53] W. He, Q. Li, Y. Sun, X. Xi, Y. Zhang, Q. Yan, *J. Mater. Chem. C* **2017**, *5*, 2459.
[54] H. J. Lee, S. Zhang, J. Luo, F. Li, T. R. Shrout, *Adv. Funct. Mater.* **2011**, *20*, 3154.
[55] P. Finkel, A. Amin, S. Lofland, J. Yao, D. Viehland, *Phys. Status Solidi A* **2012**, *209*, 2108.
[56] D. Phelan, E. E. Rodriguez, J. Gao, Y. Bing, Z.-G. Ye, Q. Huang, J. Wen, G. Xu, C. Stock, M. Matsuura, P. M. Gehring, *Phase Transitions* **2015**, *88*, 283.
[57] G. Xu, Z. Zhong, Y. Bing, Z.-G. Ye, C. Stock, G. Shirane, *Phys. Rev. B* **2003**, *67*, 104102.
[58] C. J. Howard, H. T. Stokes, *Acta Crystallogr., Sect. A: Found. Adv.* **2004**, *61*, 93.
[59] D. D. Viehland, E. K. H. Salje, *Adv. Phys.* **2014**, *63*, 267.
[60] J. Zhang, C. C. Tasan, M. J. Lai, A.-C. Dippel, D. Raabe, *Nat. Commun.* **2017**, *8*, 93.
[61] M. G. Cain, *Characterisation of Ferroelectric Bulk Materials and Thin Films*, Springer, Dordrecht, The Netherlands **2014**.
[62] J. Erhart, *Phase Transitions* **2006**, *77*, 989.
[63] S. Mantri, J. Daniels, *J. Am. Ceram. Soc.* **2021**, *104*, 1619.
[64] E .A. Patterson, M. Staruch, B. Matis, S. Young, S. E. Lofland, L. Antonelli, F. Blackmon, D. Damjanovic, M. G. Cain, P. B. J. Thompson, C. A. Lucas, P. Finkel, *Appl. Phys. Lett.* **2020**, *116*, 222903.
[65] C. Vecchini, P. Thompson, M. Stewart, A. Muñiz-Piniella, S. R. C. McMitchell, J. Wooldridge, S. Lepadatu, L. Bouchenoire, S. Brown, D. Wermeille, O. Bikondoa, C. A. Lucas, T. P. A. Hase, M. Lesourd, D. Dontsov, M. G. Cain, *Rev. Sci. Instrum.* **2015**, *86*, 103901.
[66] V. A. Solé, E. Papillon, M. Cotte, P. Walter, J. Susini, *Spectrochim. Acta, Part B* **2007**, *62*, 63.
[67] A. G. A. Nisbet, G. Beutier, F. Fabrizi, B. Moser, S. P. Collins, *Acta Crystallogr., Sect. A: Found. Adv.* **2015**, *71*, 20.
[68] Object Research Systems Inc., Dragonfly Software v2020.2, 2020.